

Simulation of radiation damping in rings, using stepwise ray-tracing methods

F. Méot
(*fmeot@bnl.gov*)

BNL C-AD, Upton, LI, NY 11973

February 25, 2014

Abstract

The ray-tracing code Zgoubi computes particle trajectories in arbitrary magnetic and/or electric field maps or analytical models. The code is a genuine compendium of numerical recipes allowing the simulation of most types of optical elements encountered in beam optics. It contains a built-in fitting procedure, spin tracking, many Monte Carlo processes. The high accuracy of the integration method allows efficient multi-turn tracking in periodic machines. Energy loss by synchrotron radiation, based on Monte Carlo techniques, has been introduced in Zgoubi in the early 2000s for the purpose of studying effects of stochastic radiation on particle dynamics in the linear collider beam delivery system, and duly benchmarked in that context. However, only recently has this Monte Carlo tool been subject to benchmarking in rings. This recent work is reported here.

1 Introduction

The ray-tracing code Zgoubi [1, 2] has recently been subject to benchmarking regarding synchrotron radiation (SR) damping in rings. Stochastic SR was first introduced in Zgoubi in 2000 [3], for assessing emittance perturbation in the beam delivery system of the “Tesla Test Facility” (an early, European, test version of the “Linear Collider”). These developments were based on methods implemented earlier in the DYNAC dynamics code developed at Saclay [4] as a design tool for the recirculating arcs in the “ALS” and “ELFE” electron recirculator projects [5, 6]. However, although presumably straightforwardly operational in rings, since ray-tracing in rings does not differ from ray-tracing in beam lines, the correctness of damping effects still had to be checked. This is the subject of the present benchmarking study and will be discussed in detail.

The benchmarking work reported here is in particular motivated by on-going activities regarding high energy machine projects as the electron-ion collider eRHIC [7] at BNL (RHIC is the relativistic heavy ion collider), which also require spin tracking, a capability of Zgoubi [8] which had motivated its use in recent design studies regarding the e^+e^- asymmetric collider project super-B [9]. It is planned, in a near future, to further report on similar thorough benchmarking of SR effects on spin dynamics in electron recirculators and in rings, including spin diffusion, in accompaniment to the on-going use of the code in design studies regarding a “fixed field alternating gradient” version of the eRHIC arcs [10].

2 The ray-tracing code Zgoubi

2.1 Introduction

The ray-tracking code Zgoubi [1] (see also Ref. [2]) computes trajectories of charged particles in arbitrary number, in analytical models of fields and/or in magnetic or electric field maps. The code is a genuine compendium of numerical recipes for the simulation of most types and geometries of optical elements encountered in beam lines, spectrometers, and periodic machines. It contains a built-in fit procedure, spin tracking, in-flight decay and several other Monte Carlo process simulations. It also provides synchrotron radiation calculation, on the one hand the spectral-angular radiation from particle motion, used for instance to understand and fix issues of negative interferences at LEP [11], and for the design of the SR based beam profile monitoring installations at LHC [12], on the other hand the energy loss and dynamical effects on particle motion, the subject of this report. SR capabilities include the handling of undulator radiation [12, 13, 14]. Development of coherent synchrotron radiation modelling has been undertaken in the early 2000s, in view of bunch compression chicane design studies, yet not released so far. The high accuracy of the numerical integration method in Zgoubi, as addressed in the next section, is well illustrated in recent tracking simulations requiring tens of thousands of turns for the study of polarized proton beam transport through strong depolarizing snake resonances at the RHIC collider [15], including full acceleration cycle simulations, 150000 turns about, in RHIC injector, the alternating gradient synchrotron (AGS) [16].

2.2 Integration of the equations of motion

The Lorentz equation, which governs the motion of a particle of charge q , relativistic mass m and velocity \vec{v} in electric and magnetic fields \vec{e} and \vec{b} , is written

$$\frac{d(m\vec{v})}{dt} = q(\vec{e} + \vec{v} \times \vec{b}) \quad (1)$$

In Zgoubi the integration variable is the arc length along the particle trajectory, s , the trajectory length element is $ds = v dt$. Noting $()' = d()/ds$ and taking

$$\vec{u} = \frac{\vec{v}}{v}, \quad \vec{u}' = \frac{d\vec{u}}{ds}, \quad m\vec{v} = mv\vec{u} = qB\rho\vec{u} \quad (2)$$

with $B\rho$ the rigidity of the particle, this equation can be rewritten under the form in which it is handled in the code, namely

$$(B\rho)' \vec{u} + B\rho \vec{u}' = \frac{\vec{e}}{v} + \vec{u} \times \vec{b} \quad (3)$$

From position $\vec{R}(M_0)$ and unit velocity $\vec{u}(M_0)$ at point M_0 , position $\vec{R}(M_1)$ and unit velocity $\vec{u}(M_1)$ at point M_1 following a displacement Δs (figure 1), are obtained from truncated Taylor expansions

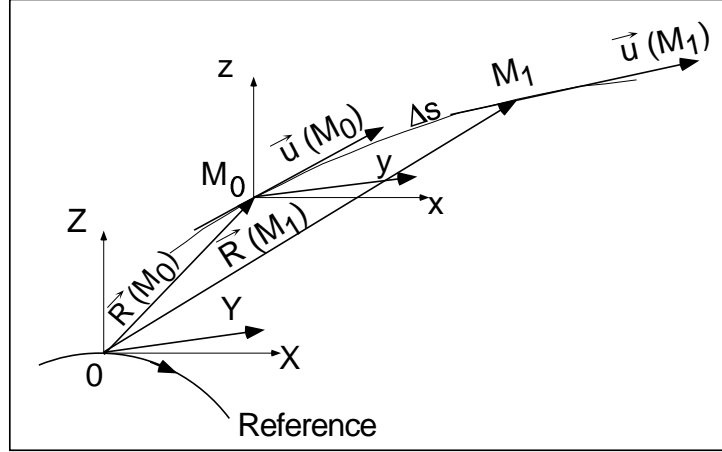


Figure 1: Particle motion in the Zgoubi frame, and parameters used in the text. The reference frame in Zgoubi has its origin in the bend plane on a reference curve which generally (but not necessarily) coincides with the optical axis in dipoles and lenses.

$$\begin{aligned} \vec{R}(M_1) &\approx \vec{R}(M_0) + \vec{u}(M_0) \Delta s + \vec{u}'(M_0) \frac{\Delta s^2}{2!} + \dots + \vec{u}''''(M_0) \frac{\Delta s^6}{6!} \\ \vec{u}(M_1) &\approx \vec{u}(M_0) + \vec{u}'(M_0) \Delta s + \vec{u}''(M_0) \frac{\Delta s^2}{2!} + \dots + \vec{u}''''(M_0) \frac{\Delta s^5}{5!} \end{aligned} \quad (4)$$

In the presence of electric fields the rigidity at M_1 is obtained in a similar way from

$$(B\rho)(M_1) \approx (B\rho)(M_0) + (B\rho)'(M_0) \Delta s + \dots + (B\rho)''''(M_0) \frac{\Delta s^5}{5!} \quad (5)$$

The expansion for the time of flight is written, similarly,

$$T(M_1) \approx T(M_0) + T'(M_0) \Delta s + T''(M_0) \frac{\Delta s^2}{2} + \dots + T''''(M_0) \frac{\Delta s^5}{5!} \quad (6)$$

The derivatives $\vec{u}^{(n)} = d^n \vec{u} / ds^n$ and $(B\rho)^{(n)} = d^n (B\rho) / ds^n$, $T^{(n)} = d^n T / ds^n$, involved in these expressions are obtained from the electric and magnetic fields and their derivatives, $\vec{e}^{(n)}$, $\vec{b}^{(n)}$, by recursive differentiation of the equation of motion (3) (see Ref. [2] for details). In this work however we will only be concerned with stepwise integration in magnetic optical structures.

Note that in Zgoubi the unit velocity vector is handled under the form

$$\vec{u} = [\cos(P) \times \cos(T), \cos(P) \times \sin(T), \sin(P)] \quad (7)$$

with T its angle with respect to the vertical, Z axis (Fig. 1), and P the angle that its projection in the (X, Y) plane does with the X axis. This maintains its unitary modulus, at each integration step.

2.3 Synchrotron radiation in Zgoubi

Synchrotron radiation (SR) effects are introduced by modifying the particle energy at the end of an integration step.

Provision has been made in addition, to allow accounting for angle scattering, however the effect is small and not included in the present study. The next sections describe the main aspects of the method, more can be found in appendix A and Ref. [2], a general treatment of the theory can be found in Ref. [17].

2.3.1 Energy loss

Given a particle travelling in the magnetic field of an arbitrary optical element or field map, Zgoubi will compute the energy loss due to stochastic photon emission, and so update the particle momentum as a result of that effect, at each integration step. The energy loss is calculated in a classical manner, based on two random processes, namely,

- probability of emission of one or more photons over an integration step,
- energy of the emitted photon(s).

The effects on particle dynamics are either limited to the alteration of energy, or may include scattering (namely, a change in the direction of the momentum vector due to the angle of emission of the photon with respect to that vector), in which case a third random process,

- the photon emission angle,

may be accounted for.

2.3.2 Dynamical effects

The correction to the particle energy is obtained by summation of the individual energies (Eq. 34) of the k photons (Eq. 32) emitted along Δs .

SR statistics in uniform field will therefore converge towards the following averages :

- energy loss ¹ by an electron of energy E , over a step $\Delta s = \rho \Delta \theta$ (considering constant curvature radius, $\rho = B\rho/B$, over the arc of trajectory $\Delta \theta$, with B the local field value),

$$\Delta E = \frac{2}{3} r_0 E_0 \gamma^4 \frac{\Delta \theta}{\rho} = \frac{2}{3} r_0 e c \gamma^3 B \Delta \theta \quad (8)$$

with $r_0 = e^2 / 4\pi \epsilon_0 m_0 c^2$ the classical radius of the electron, e the elementary charge, m_0 the electron rest mass, $\epsilon_0 = 1 / 36\pi 10^9$, $E_0 = m_0 c^2$ the rest energy, $\gamma = E/E_0$;

- energy spread ²,

$$\sigma_{\Delta E/E} = \frac{\sqrt{110\sqrt{3}\hbar c / \pi \epsilon_0}}{24E_0/e} \gamma^{5/2} \frac{\sqrt{\Delta \theta}}{\rho} \quad (9)$$

Note that, unless otherwise specified, notations in this study assume $\beta = v/c = 1$.

2.3.3 Benchmarking, preliminary steps

At this stage, the installation of the Monte Carlo machinery in Zgoubi can be benchmarked for these quantities, using, following the hypotheses in appendix B, $\rho = 24.95549$ m and iso-magnetic lattice. From a practical point of view, in order to stick to ideal theoretical conditions, a single bend is tracked once-through, so to avoid such effects as orbit spiraling, momentum spread, that may be sensible over a large ring or in presence of RF compensation.

Results are given in Tab. 1. The classical, theoretical formulæ used are recalled in the rightmost column. E_s is the total energy of the reference particle, $\mathcal{C}_\gamma = \frac{4\pi}{3} \frac{r_0}{(m_0 c^2)^3}$. The values so computed are for 6 GeV kinetic energy, they are converged numerically, up to the last digit shown in the table, in terms of the integration step size in the bend ($\Delta s = 1$ cm in Eq. 4) and of the number of radiated photons (made large enough, via the number of passes), this is shown in figure 12, appendix C.

It can be seen that the agreement between Zgoubi tracking data (col. 3 in Tab. 1) and theoretical expectations (col. 4) is very good, this is a first step towards validation the SR Monte Carlo installation in Zgoubi. Monte Carlo losses at higher energies are further shown to yield as good agreement with Eq. 8, in Tab. 7.

¹An other form of the familiar relation $\Delta E/E \approx 1.88 \cdot 10^{-15} \gamma^3 \Delta \theta / \rho$.

²Which writes $\sigma_{\Delta E/E} = 3.80 \cdot 10^{-14} \gamma^{5/2} \sqrt{\Delta \theta} / \rho$, for electrons.

Table 1: Preliminary benchmarking : SR loss characteristics in the Chasman-Green cell defined in Tab. 9, appendix B. These quantities have been computed from a large number of once-through passes, of a 3000 particle batch, in a single dipole, they are shown scaled to a full turn (64 such dipoles).

Kinetic energy 6 GeV	Units	Zgoubi tracking	Theory value	formula (SI units)
Energy loss, U_s	MeV / turn	4.59565	4.59565	$\frac{C_\gamma}{2\pi} E_s^4 \oint \frac{ds}{\rho(s)^2} \stackrel{iso-\rho}{=} C_\gamma \frac{E_s^4}{\rho}$
Critical photon energy, ϵ_c	keV	19.2049	19.2051	$\frac{3\hbar\gamma^3 c}{2\rho}$
Average photon energy, $\bar{\epsilon}$	keV	5.9136	5.9136	$\frac{8}{15\sqrt{3}} \epsilon_c$
Nb. of average photons	/turn/particle	777.12	777.12	$U_s/\bar{\epsilon}$
<i>rms</i> energy spread, $\sqrt{(\epsilon - \bar{\epsilon})^2}$	keV	10.7375	10.7375	$\frac{\sqrt{211}}{15\sqrt{3}} \epsilon_c$

2.3.4 Scattering

Trajectory scattering may assume for simplicity a cylindrical-symmetric Gaussian distribution

$$p(\xi) = \exp\left(-\frac{\xi^2}{2\sigma_\xi^2}\right) \quad (10)$$

of the photon emission angle ξ with respect to the particle velocity. For simplicity as well σ_ξ may be considered independent of photon energy ϵ , with value $\approx 1/\gamma$. Whether these two approximations hold may be problem dependent, however these hypotheses may easily be improved in the code if this is found necessary.

Accounting for scattering is an option in Zgoubi. Since its effect on beam divergence is very small in the present benchmarking conditions (mainly a matter of asymptotic vertical invariant value), it does not need be (and is not) taken into account.

2.3.5 Field scaling

Particle stiffness decrease upon SR loss entails perturbation of focusing properties due to increased strength of the magnets. In the case of single-pass beam lines, this effect may be taken care of, resulting in the scaling of magnetic fields to the *theoretical* average energy loss, namely (Eq. 8)

$$\Delta E_{scaling} = \sum_{bends} \frac{2}{3} r_0 e c \gamma^3 B \Delta\theta \quad (11)$$

Note the following : (i) using that analytical expression in computing the scaling coefficient is preferred to the average energy loss from the tracked particle population, since in the latter case it would make it dependent on the accuracy of the statistics ; (ii) on the other hand, doing so the contribution of other magnets (quadrupoles, sextupoles, etc.) is not accounted for in the scaling, in the present state of Zgoubi coding, however this can easily be modified in the code if useful.

In storage rings, bends and lenses are normally operated at fixed field, whereas the RF takes care of restoring the energy lost. In pulsed regime as in booster injectors, the same process of energy recovery by the RF holds, thus requiring no particular measures on Zgoubi simulations side, save *ad hoc* synchronous RF phase considerations.

3 Benchmarking method

Benchmarking of the Monte Carlo SR in Zgoubi is based on the monitoring of the only data Zgoubi can produce : particle coordinates, versus time or turn number, and of quantities derived from these, as motion excursions, invariants, concentration ellipses (see appendix D). The quantities investigated here are explicated in section 3.1, all outcomes will eventually be compared with theoretical expectations. Note that in the text, unless otherwise specified, emittances are taken *rms*, unnormalized.

3.1 Motion invariants

In the absence of perturbation by synchrotron radiation, particle motion satisfies the following invariants,

$$\epsilon_z = \gamma_z(s)z^2 + 2\alpha_z(s)zz' + \beta_z(s)z'^2 \quad \text{Courant-Snyder} \quad (12)$$

$$\epsilon_l = \frac{\alpha E_s}{2\Omega_s} \left[\left(\frac{\Delta E}{E_s} \right)^2 + \frac{1}{\Omega_s^2} \left(\frac{d}{dt} \frac{\Delta E}{E_s} \right)^2 \right] \quad \text{longitudinal} \quad (13)$$

$$(\widehat{\Delta E})^2 = (\Delta E)^2 + \frac{1}{\Omega_s^2} \left(\frac{d\Delta E}{dt} \right)^2 \quad \text{synchrotron amplitude squared} \quad (14)$$

with $z = x$ or y the horizontal or vertical transverse coordinate, β_z and $\alpha_z = -\beta'_z/2$ the Twiss parameters, $\Delta E = E - E_s$ the energy offset, E_s the reference energy, $\Omega_s^2 = -\omega_{\text{rev}}^2 \eta h_{\text{RF}} e \hat{V} \cos \phi_s / 2\pi E_s$ the synchrotron angular frequency, with $\eta = 1/\gamma^2 - \alpha \approx \alpha$ the phase slip factor, α the momentum compaction. h_{RF} is the RF harmonic, $\omega_{\text{rev}} = 2\pi/T_{\text{rev}}$ the revolution angular frequency, \hat{V} the RF peak voltage, ϕ_s the synchronous phase (numerical values considered for these latter quantities in the benchmarking exercises to follow are given in Tab. 10, appendix B).

Introducing the squared *rms* relative synchrotron amplitude $\sigma_{\frac{\Delta E}{E}}^2 \equiv (\widehat{\Delta E}/E_s)^2$, Eqs. 13 and 14 lead to the following relationship

$$\epsilon_l = \frac{\alpha E_s}{2\Omega_s} \sigma_{\frac{\Delta E}{E}}^2 \quad (15)$$

Note that in the present simulations, particle motion is observed in a non-dispersive region in the cell (namely, at the azimuth $s = 0$ in Fig. 10, appendix B), thus there is no need to subtract the effect of the dispersion function on the horizontal phase space coordinates, when estimating the emittances from the tracking.

Under the effect of stochastic SR, individual invariants can in general not be determined, averages over particle ensembles are considered instead, they evolve according to

$$\frac{d\bar{\epsilon}_n}{dt} = -\frac{\bar{\epsilon}_n}{\tau_n} + C_n \quad (16)$$

$\overline{(\ast)}$ denotes the average over particles ; $\epsilon_n = \epsilon_x, \epsilon_y$ or ϵ_l ; at fixed energy (storage ring) C_n is a constant, characteristic of the quantum excitation, which will be explicated in due place) towards a stationary solution

$$\epsilon_{n,eq} = C_n \tau_n \quad (17)$$

with damping time

$$\tau_n = \frac{T_{\text{rev}} E_s}{U_s J_n} \quad (18)$$

with $J_{n=x,y,l}$ the partition numbers, respectively horizontal, vertical, longitudinal, which, in passing, satisfy (the Robinson theorem)

$$J_x + J_y + J_l = 4 \quad (19)$$

Note that the present benchmarking simulations consider for simplicity a planar ring (see appendix B), with the effect that the vertical motion is not subject to chromatic orbit fluctuations, by contrast with the horizontal betatron motion which experiences orbit fluctuations upon stochastic energy loss. It is thus possible to compute the vertical invariant and follow its smooth evolution turn by turn, from a single particle tracking, this will be addressed specifically in the next section.

4 Damping simulations

Based on the working hypotheses and methods discussed in section 3, series of multi-turn tracking simulations have been performed for the benchmarking of Zgoubi synchrotron radiation Monte Carlo machinery. They are summarized in the next two sections, in the form in particular of series of figures and tables.

4.1 Damping of the vertical motion

The vertical motion is considered first, using single particle tracking following the planar ring hypotheses as discussed in section 3. A 18 GeV particle is launched for 500 turns (10 damping times about) in the 16-cell ring. Since there is no vertical dispersion, its vertical phase space coordinates y, y' are expected to show no stochastic fluctuation, as confirmed by the smoothly spiralling phase space motion observed in Fig. 2. From these coordinates the vertical invariant can be computed, namely,

$$\epsilon_y = \gamma_y y^2 + 2\alpha_y y y' + \beta_y y'^2 \quad (20)$$

with local Twiss parameter values at the observation point $\beta_y = 11.303$, $\alpha_y = 0$, $\gamma_y = 1/\beta_y = 0.0885$ (see Tab. 9, bottom rows). The invariant ϵ_y is expected to damp exponentially towards zero, with a damping time (Eq. 18 with $J_y = 1$)

$$\tau_y = \frac{T_{rev} E_s}{U_s} \approx 0.13114 \text{ ms}, \quad \text{or} \quad \tau_y = \frac{E_s}{U_s} \approx 48.06 \text{ turns} \quad (21)$$

given $E_s = 18 \text{ GeV}$, $T_{rev} = 2.711216 \mu\text{s}$ (independent of the starting invariant and of the turn, following the tracking outcomes), whereas (see Tab. 7) theoretical energy loss $U_s = 372.16 \text{ MeV/turn}$.

This is confirmed in Fig. 3 which shows smooth exponential damping of the vertical invariant on the one hand, in four different cases of starting initial invariant values yielding on the other hand damping times given in Tab. 2, which are in accord with Eq. 21 in a 2 per mill range.

Table 2: Vertical damping times for four different vertical invariants, single particle tracking.

Starting invariant (nm.rad, non normalized)	Damping time (turns)
10^3	48.056
10	48.144
10^{-1}	48.000
10^{-5}	48.103

Additional simulation results concerning the vertical motion will be produced in the next section.

4.2 Emittance damping

Multi-particle tracking is now investigated, considering a large starting emittance (in order essentially to clearly show the damping, a different choice could have been to start from a zero emittance and let it grow), in either one of the three planes, horizontal, vertical or longitudinal. The tracking is carried out up to equilibrium, $\epsilon_{n,eq}$, i.e., a few damping times away.

Four different energies are considered : 6, 9, 12 and 18 GeV, kinetic.

For all three motions, transverse and longitudinal, the evolution of the emittance with time or turn number, t , is expected to satisfy

$$\bar{\epsilon}_n(t) = \epsilon_{n,eq} (1 - e^{-t/\tau_n}) + \epsilon_{n,i} e^{-t/\tau_n} \quad (n = x, y, \text{ or } l) \quad (22)$$

with $\epsilon_{n,i}$ and $\epsilon_{n,eq}$ respectively the starting and equilibrium emittances.

The cases of the longitudinal and horizontal motions are illustrated in figures 4 and 5 respectively, which show the good matching between Zgoubi tracking (5000 particles for each energy), and Eq. 22. The matching yields the equilibrium values $\epsilon_{l,eq}$, $\epsilon_{x,eq}$, and damping times, τ_l , τ_x , as reported in Tabs. 4, 6, 7.

On the other hand, since these simulations consider a planar ring, the vertical emittance damps to zero, as discussed in section 4.1, i.e., $\epsilon_{y,eq} \rightarrow 0$, so yielding

$$\bar{\epsilon}_y(t) = \epsilon_{y,i} e^{-t/\tau_y} \quad \text{and} \quad \ln(\bar{\epsilon}_y(t)) = \ln(\epsilon_{y,i}) - \frac{t}{\tau_y} \quad (23)$$

This produces the results displayed in Fig. 6 which shows the smooth damping, as due to the absence of fluctuations in the vertical motion in the absence of vertical dispersion, for a 2000 particle bunch tracked for 10 damping times about, in the four different cases 6, 9, 12 and 18 GeV. A linear regression on the logarithmic set of turn-by-turn emittances $\bar{\epsilon}_y(t)$ yields the matching straight line as displayed, for each energy, of which the absolute value of the inverse slope is the damping time, values as reported in Tab. 7, rightmost column. The agreement with the theory is good, at percent level. The phase space angle

$$\phi_y = \text{atan} \frac{\alpha_y y + \beta_y y'}{y} \quad (24)$$

is also recorded, it is expected to feature a uniform density distribution in the $[-\pi, \pi]$ interval, which Fig. 7 shows to be fairly satisfied.

Uniform distributions as well, not worked out here, are expected for the horizontal phase space angle ϕ_x , as well as for the longitudinal angle

$$\phi_l = \text{atan} \frac{d\Delta E/dt}{\Omega_s \Delta E} \quad (25)$$

Other possible tests concern the beam centroids, expected to damp to zero with damping times $2\tau_n$, this has been checked to be satisfied, on various cases, not reported here. The equilibrium distribution of any of the phase space variables, x , x' , ΔE , etc. is also a test of the correctness of the SR process simulation, they have to match Gaussian densities, with rms width for instance (various values have been benchmarked, reported in Tab. 6),

$$\sigma_x(s) = \left(\beta_x(s) \frac{C_q \gamma^2}{J_x \rho} \bar{\mathcal{H}} + D_x^2(s) \sigma_{\frac{\Delta E}{E}}^2 \right)^{1/2}, \quad \sigma_{\frac{\Delta E}{E}} = \frac{1}{\sqrt{2}} \sigma_{\widehat{\frac{\Delta E}{E}}} = \sqrt{\frac{C_q}{J_l \rho}} \gamma \quad (26)$$

with $D_x(s)$ the local dispersion.

A note on damping without fluctuations : The horizontal and longitudinal damping times could be obtained with high accuracy by tracking a single particle and accounting for the energy loss *on average, without fluctuations*, instead (just like for the vertical invariant, as a consequence of the present hypothesis of a planar ring, as addressed

207 in section 4.1). A matching of the turn-by-turn evolution of the invariant (respectively, Eq. 12 with $z = x$ and
 208 Eq. 13) would then provide the damping time as the absolute value of the inverse slope of the straight line repre-
 209 senting $\ln(\bar{\epsilon}_n(turn))$ ($n = x$ or l), given that $\epsilon_{n,eq} = 0$ in the absence of stochasticity. However it is a deliberate
 210 choice here to benchmark the code in realistic situation, in the presence of stochastic photon emission using the
 211 Monte Carlo machinery installed for that. The counterpart is that it requires a two-variable matching : damping
 212 time and final emittance. It is left to the interested user, as a further benchmarking test, to replace (in the code) the
 213 Monte Carlo stochastic energy loss by the average energy loss, and then verify the exponential damping of a single
 214 particle invariant, in that special configuration of the Zgoubi machinery.

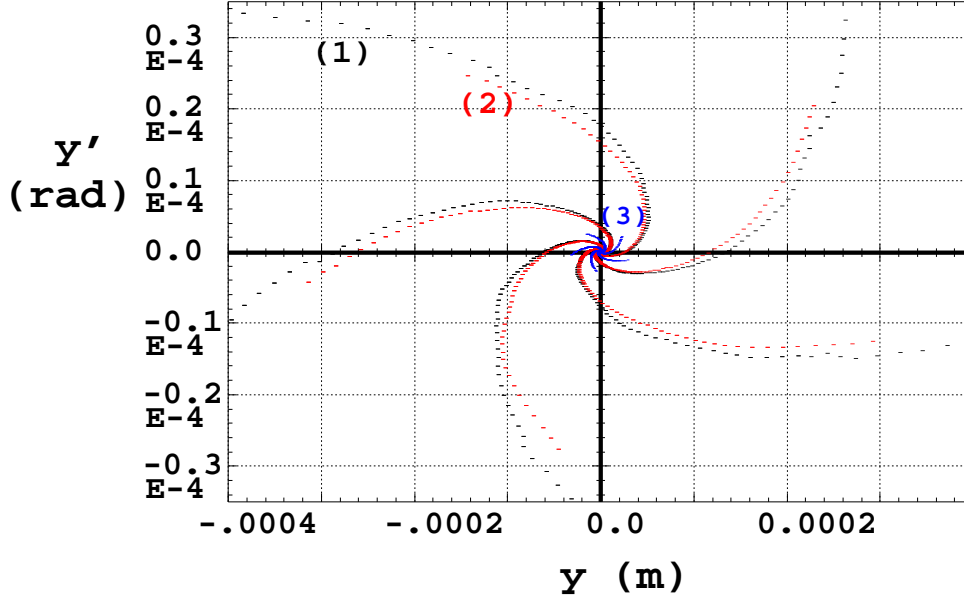


Figure 2: Vertical phase space of four particles with different starting invariants, 18 GeV (as detailed in Fig. 3 - motion of particle 4 is too small to be visible here). Motions are observed over 500 turns at $s = 0$ (s is defined in Fig. 10).

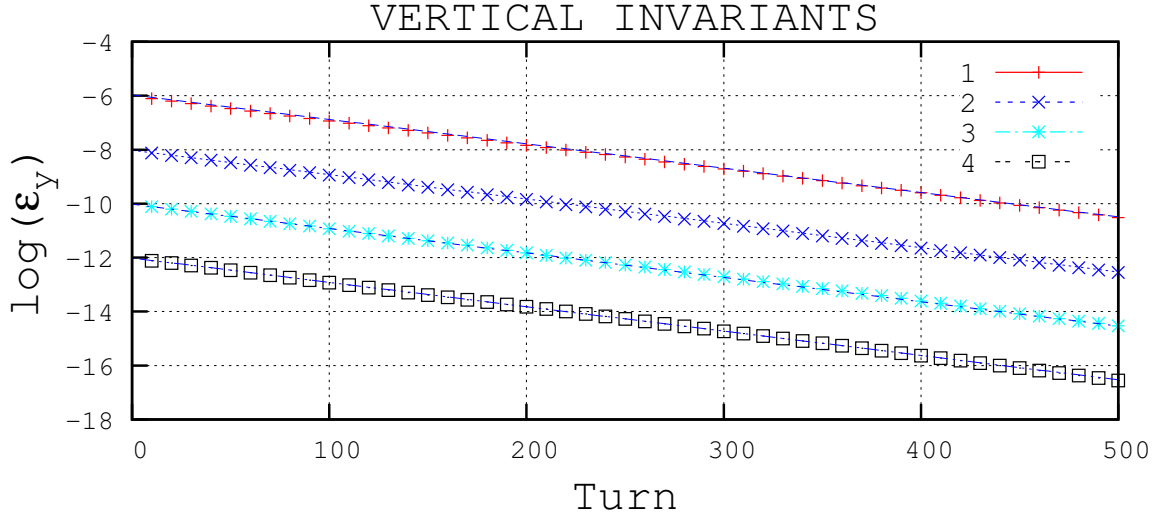


Figure 3: Exponential damping of the vertical invariant ϵ_y (Eq. 20), over 500 turns, 18 GeV, case of four particles with different starting invariant values, respectively, from 1 to 4 : 10^3 , 10, 10^{-1} , 10^{-3} nm.rad.

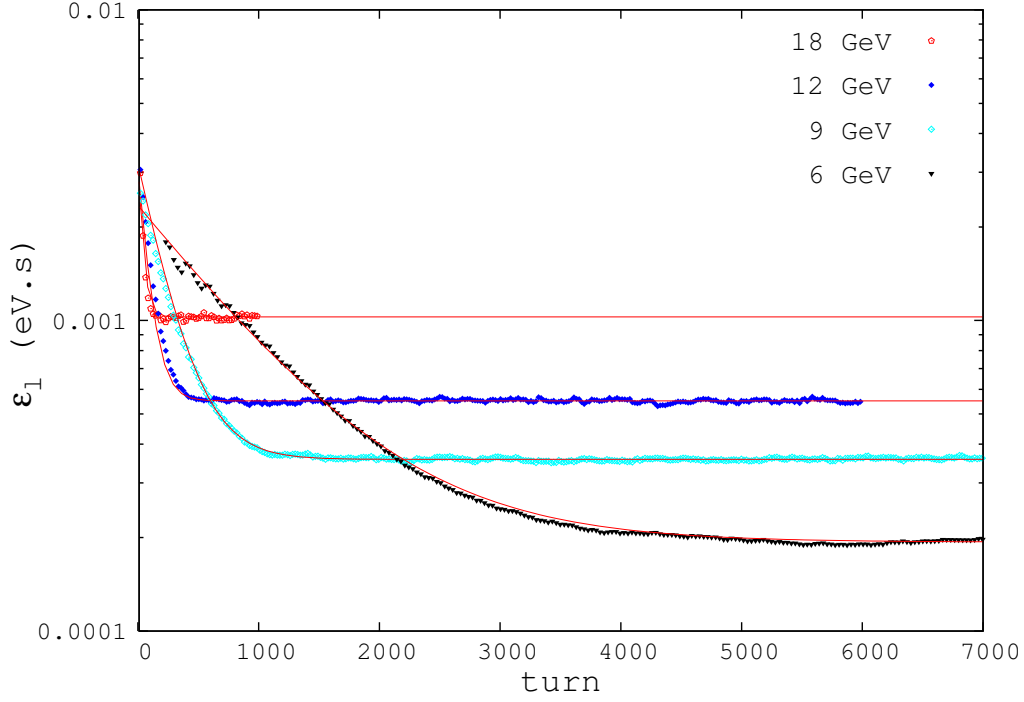


Figure 4: Evolution of the longitudinal emittance with the number of turns, in four different cases of energy, 6, 9, 12 and 18 GeV. Markers are from tracking (plotted every 20 turns about), solid lines are from matching with the exponential law (Eq. 22). Damping times in Tabs. 4, 7 have been determined from these data.

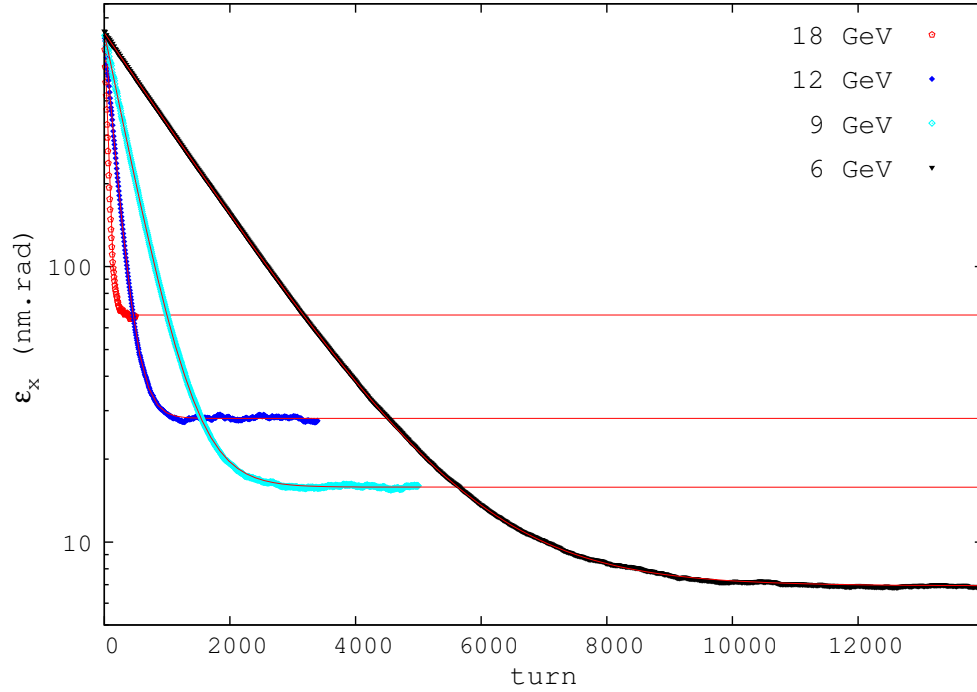


Figure 5: Evolution of the horizontal emittance with the number of turns, in four different cases of energy, 6, 9, 12 and 18 GeV. Markers are from tracking (plotted every 20 turns about), solid lines are from matching with the exponential law (Eq. 22). Damping times in Tabs. 4, 7 have been determined from these data.

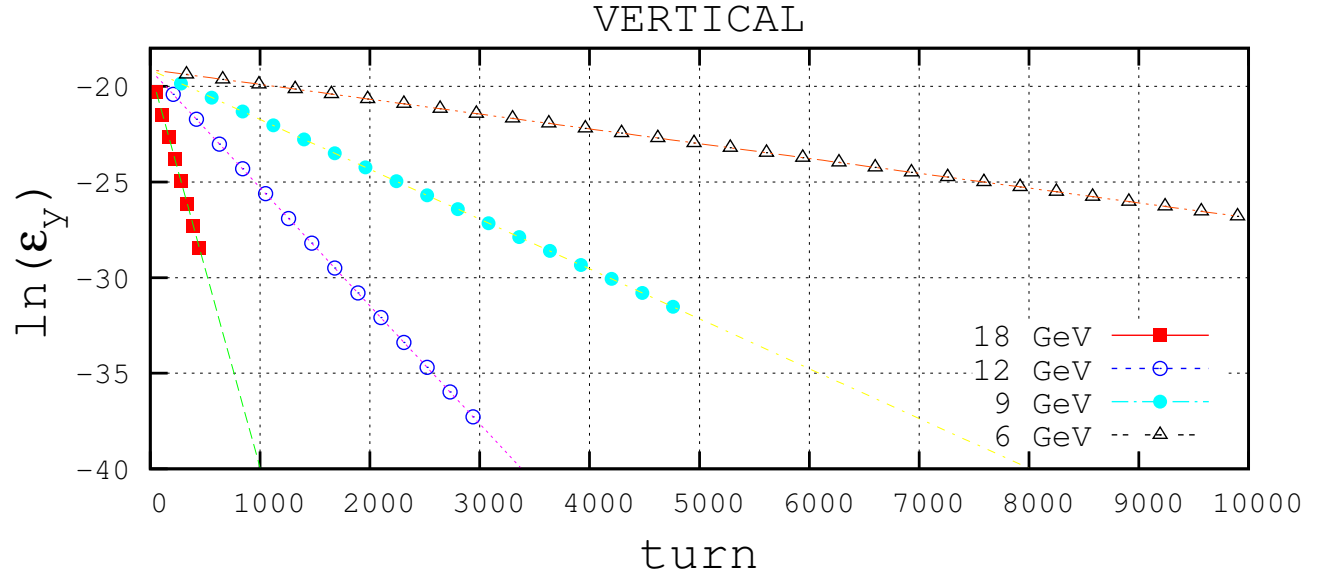


Figure 6: Smooth evolution of the vertical emittance towards zero, for 6, 9, 12 and 18 GeV, 2000 particles. Markers are from the tracking, straight lines are from the exponential match (Eq. 23), with inverse slope absolute values as reported in Tab. 7.

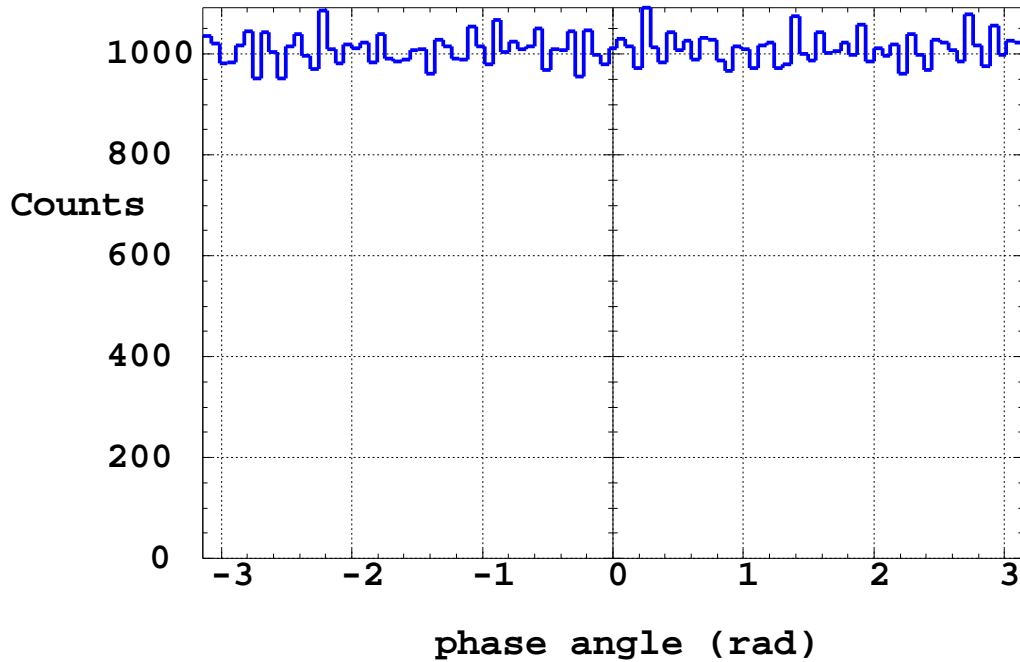


Figure 7: Histogram of the phase space angle (Eq. 24) over 10^5 particle phase space positions after a few damping time tracking, beam energy 12 GeV.

A series of summary tables

Numerical results from Zgoubi tracking for 6 GeV electron kinetic energy are displayed in Tabs. 3-5. Up to 3000 or 6000 particles have been tracked depending on the exercise, up to several damping times. Several runs, however in rather limited number, have been performed in each case, with various initial conditions, random generator seeds, this will not be detailed here. Due to the limited number of trials, error bars can be up to a few percent level, depending on the parameters of concern, which is anyway considered indicative of the correct behavior of Zgoubi in matter of SR simulation and its effects.

In addition to Zgoubi tracking and to theoretical formulæ, the light source code BETA [18] developed at Saclay is used in this benchmarking, as a follow on of the above mentioned initial work in Ref. [3]. Determination of SR parameters in BETA is based on the computation of the radiation integrals, from the lattice parameters.

Tab. 3 aims at showing that the SR integrals can be recovered from the tracking, which may be useful in case of non-zero orbit, varying curvature, strong momentum deviation, etc., as for instance in the case of FFAG type of lattices, as presently under study [10].

Tab. 4 gives the numerical values of the damping times for the three motions, drawn from the tracking, and their theoretical value in the case of the Chasman-Green cell.

Tab. 5 gives the damping partition number, in a similar manner both from tracking and from theoretical formulæ.

Tab. 6 gives the equilibrium quantities, including emittances, energy spread, bunch lengthening.

Table 3: SR integrals. In the “Theory” column, numerical values are derived from the the reduced expressions for an *iso-magnetic* lattice, at the right of the left column integrals. In the “Ray-tracing” column, values have been derived indirectly, following the recipes given in footnote and using the numerical values of damping times and equilibrium quantities reported in Tabs. 4, 6, as obtained from Zgoubi tracking in the 16-cell ring.

($\oint \equiv$ integral over the dipoles)		Units	Theory	Ray-tracing
$I_1 = \oint \frac{D_x}{\rho(s)} ds$	$= \alpha \mathcal{C}$	(m)	0.2516	0.250 ^(c)
$I_2 = \oint \frac{ds}{\rho(s)^2}$	$= \frac{2\pi}{\rho}$	(m ⁻¹)	0.2518	0.253 ^(d)
$I_3 = \oint \frac{ds}{ \rho(s) ^3}$	$= \frac{2\pi}{ \rho ^2}$	(10 ⁻² m ⁻²)	1.0089	1.017 ^(e)
$I_4 = \oint \frac{D_x}{ \rho(s) ^3} (1 - 2n) ds$	$= \frac{1}{ \rho ^3} \oint D_x ds$ ^(a)	(10 ⁻⁴ m ⁻¹)	4.26	≈ 5 ^(f)
$I_5 = \oint \frac{\mathcal{H}}{ \rho(s) ^3} ds$	$= \frac{2\pi}{ \rho ^2} \bar{\mathcal{H}}$ ^(b)	(10 ⁻⁵ m ⁻¹)	3.2562	3.271 ^(g)
$\bar{\mathcal{H}} = \frac{1}{2\pi\rho} \oint_{bends} \mathcal{H} ds$	$\stackrel{(CG)}{=} \rho \theta^3 (\frac{\gamma_0 \mathcal{L}}{20} + \frac{\beta_0}{3\mathcal{L}} - \frac{\alpha_0}{4})$ ^(b)	(10 ⁻³ m)	3.2209	3.207 ^(h)

(a) $n = -\rho/B \partial B/\partial x$ field index, zero here, ρ is the curvature radius in the bends.
(b) $\mathcal{H} = \gamma_x D_x^2 + 2\alpha_x D_x D'_x + \beta_x D'^2_x$. (CG) : case of Chasman-Green lattice. D_x is the dispersion, D'_x its derivative, α, β, γ are the optical functions, the subscript “0” denotes their values at entrance to the first cell bend (see Fig. 10).
(c) From momentum compaction.
(d) From vertical damping time, τ_y , Tab. 4 : $I_2 = 3T_{rev}/(2r_0\gamma^3\tau_y)$
(e) From I_2 : $I_3 = I_2^2/(2\pi) = 0.2528^2/(2\pi)$.
(f) From I_2 and damping parameter \mathcal{D} , Tab. 5.
Note : (i) higher accuracy on \mathcal{D} would require more statistics, (ii) using damping times instead (Tab. 4) yields even greater uncertainty, since $I_4 \sim \frac{D_x}{\rho^2} \ll I_2 \sim \frac{1}{\rho}$.
(g) From I_2 and from I_5/I_2 , equilibrium ϵ_x , Tab. 6.
(h) From equilibrium ϵ_x , Tab. 6.

Table 4: Emittance damping times. They are obtained by matching the turn-by-turn emittance with equation 22, as in figures 4, 5. Agreement between Zgoubi tracking in the presence of stochastic SR on the one hand, and theoretical expectations on the other hand, is within 1-2 percent, for the three motions. The values in the “Zgoubi” column are the averages over a few trials.

	Units	BETA code	Zgoubi	Theory value	formula
horizontal, τ_x	ms	3.546	3.547	3.547	$= \frac{T_{rev} E_s}{U_s J_x} = \frac{3T_{rev}}{2r_0\gamma^3(I_2 - I_4)}$
	turns	1308	1308	1308	
vertical, τ_y	ms	3.540	3.501	3.541	$= \frac{T_{rev} E_s}{U_s J_y} = \frac{3T_{rev}}{2r_0\gamma^3 I_2}$
	turns	1306	1291	1306	
longitudinal, τ_l	ms	1.769	1.757	1.769	$= \frac{T_{rev} E_s}{U_s J_l} = \frac{3T_{rev}}{2r_0\gamma^3(2I_2 + I_4)}$
	turns	652	648	652	

Table 5: Partition numbers, damping parameter. Average values from a few trials are given. In general the theoretical value falls within that set of values. More statistics would be required for better precision, *e.g.*, so to satisfy $J_y = 1$ with higher accuracy.

	Units	BETA code	Zgoubi	Theory value	formula
J_x		0.9984	0.998 ^(a)	0.9984	$= 1 - \mathcal{D} \xrightarrow{strong\,foc.} 1^-$
J_y		1	0.998 ^(b)	1	$= 1$
J_l		2.0016	2.002 ^(c)	2.0016	$= 2 + \mathcal{D} \xrightarrow{strong\,foc.} 2^+$
Damping parameter, \mathcal{D}	10^{-3}	1.6049	1.95 ^(d)	1.6049	$= \frac{I_4}{I_2} \stackrel{n=0}{iso-\rho} = \frac{\alpha\mathcal{C}}{2\pi\rho}$
	10^{-3}	1.6049	2 ^(d)	1.6049	

(a) From τ_x value, Tab. 4 : $J_x = \frac{T_{rev} E_s}{U_s \tau_x} = \frac{2.71122 \cdot 10^{-6} \times 6000.511}{4.5956 \times \tau_x} = \frac{3.540 \cdot 10^{-3}}{3.547 \cdot 10^{-3}}$.

(b) From τ_y value : $J_y = \frac{3.540 \cdot 10^{-3}}{3.547 \cdot 10^{-3}}$, rms value at few 10^{-3} level. J_y should be unity (planar ring), better precision requires more statistics.

(c) From $\sigma_{\frac{\Delta E}{E}}$ or τ_l values.

(d) Values obtained from, respectively, $\mathcal{D} = 1 - J_x$, $J_l - 2$.

Table 6: Equilibrium quantities from tracking (“Zgoubi tracking” column). Emittances have been obtained by matching the turn-by-turn emittance with equation 22, as in figures 4, 5. Bunch lengthening and energy spreading are also given, $\sigma_{\frac{\Delta E}{E}}$ denotes the *rms* energy spread, $\sigma_{\widehat{\frac{\Delta E}{E}}}$ denotes the *rms* synchrotron amplitude, σ_l is the bunch lengthening. Values in the “BETA” the BETA light source code. Data in the “Theory value” column stem from the formulæ in the rightmost column.

	Units	BETA code	Zgoubi tracking ^(a)	Theory value	formula
horizontal, $\epsilon_{x,eq}$	nm.rad	6.843	6.83	6.831	$= \frac{C_q \gamma^2}{J_x} \frac{I_5}{I_2} \stackrel{iso-\rho}{=} \frac{C_q \gamma^2}{J_x \rho} \bar{\mathcal{H}} \stackrel{(b)}{(c)}$
vertical, $\epsilon_{y,eq}$	pm	-	$\rightarrow 0$	≈ 0.15	$= \frac{13}{55} \frac{C_q}{J_y I_2} \oint \frac{\beta_y}{ \rho^3 } ds$
longitudinal, $\epsilon_{l,eq}$	$\mu\text{eV.s}$	-	193.5	191.8	$= \frac{\alpha E_s}{2\Omega_s} \sigma_{\widehat{\frac{\Delta E}{E}}}^2 = \frac{\alpha E_s}{\Omega_s} \frac{C_q \gamma^2}{J_l \rho}$
rms dE/E , $\sigma_{\frac{\Delta E}{E}} = \frac{1}{\sqrt{2}} \sigma_{\widehat{\frac{\Delta E}{E}}}$	10^{-3}	1.03	1.023	1.028	$= \sqrt{\frac{C_q}{J_l \rho}} \gamma$
rms bunch length, σ_l	mm	-	9.40	9.308	$= \frac{\alpha c}{\Omega_s} \sigma_{\frac{\Delta E}{E}}$

(a) Spreading on Zgoubi quantities, over the few trials performed, are within percent.

(b) $C_q = \frac{55}{32\sqrt{3}} \frac{\hbar}{m_0 c} \approx 3.831938 \cdot 10^{-13} [\text{m}]$.

(c) This yields J_x (Tab. 5), namely, $J_x = \frac{3.831938 \cdot 10^{-13} \times 11742.683^2}{\epsilon_{x,eq} \times 24.9555 [\text{m}]} \times 3.2209 [\text{m}] = 0.9984$

Energy dependence

Benchmarking for energy dependence of equilibrium emittances and damping times is summarized in Tab. 7. Expected γ -scaling laws are recalled (3rd row), as well as energy loss (2nd column). Values between square brackets are the expected theoretical ones. A limited number of tracking trials have been realized in general for any of these quantities, their average value is displayed in the table. In spite of this limited statistics, the agreement is rather satisfactory, within a few percent or better, better in particular for the vertical motion which is not subject to stochastic motion. Differences with formulæ may have various origins, *e.g.*, oscillations due to mis-centering of the beam at injection, fluctuations with turn number due to the limited number of particles.

Table 7: Dependence of the energy loss, of damping times, and of longitudinal and horizontal equilibrium emittances, on the kinetic energy, as obtained from Zgoubi tracking, up to 10 damping times about, depending on the quantity of concern. 2000 particles have been tracked for τ_y , 5000 for the horizontal and longitudinal quantities. Values between square brackets are the theoretical expectations, following formulæ in Tabs. 1, 4, 6. It can be checked from these data that the theoretical γ -scaling rules are correctly restituted by the tracking.

	Energy loss U_s (MeV/turn)	$\epsilon_{l,eq}$ ($\mu\text{eV.s}$)	τ_l (ms)	$\epsilon_{x,eq}$ (nm.rad)	τ_x (ms)	τ_y (ms)
Scaling	γ^4	$\gamma^{3/2}$	$1/\gamma^3$	γ^2	$1/\gamma^3$	$1/\gamma^3$
6 GeV	4.5956 [4.5956]	194 [192]	1.757 [1.7685]	6.83 [6.83]	3.547 [3.5460]	3.501 [3.5400]
9 GeV	23.263 [23.263]	359 [352]	0.575 [0.5240]	15.6 [15.37]	1.020 [1.0508]	1.04 [1.0490]
12 GeV	73.518 [73.518]	545 [542]	0.222 [0.2211]	28.0 [27.32]	0.447 [0.4433]	0.439 [0.4426]
18 GeV	372.16 [372.16]	1021 [996]	0.0667 [0.0655]	65.7 [61.46]	0.132 [0.1314]	0.130 [0.1311]

5 Coupled motion

5.1 Working hypotheses

The source of induced vertical emittance is a single skew quadrupole introduced in a dispersion free drift ($s=0$, Fig. 10). The difference resonance $Q_x - Q_y = 25$ is considered, the lattice is tuned to $Q_x \approx 36.2$, $Q_y \approx 11.2$, see Fig. 11. $Q_x - Q_y - 25 = \Delta$ is the distance of the unperturbed tunes to an integer, with Δ small.

A perturbative treatment of coupling in the presence of synchrotron radiation can be found in Ref. [19]. Following Guignard's formalism, a coupling strength is defined,

$$\kappa = \frac{1}{2\pi} \oint K_s \sqrt{\beta_x \beta_y} e^{i(\psi_x - \psi_y - \Delta 2\pi s / \mathcal{C})} ds \quad (27)$$

with $K_s = \frac{1}{2B\rho} \left(\frac{\partial B_x}{\partial x} - \frac{\partial B_y}{\partial y} \right)$ the skew quadrupole strength, $\beta_{x,y}$ (respectively $\psi_{x,y}$) the local uncoupled horizontal and vertical betatron functions (phase advances) at the skew quadrupole, \mathcal{C} the ring circumference. In the presence of a single skew quadrupole Eq. 27 yields the approximation

$$|\kappa| \approx \frac{|K_s L|}{2\pi} \sqrt{\beta_x \beta_y} \quad (28)$$

with $K_s L$ the integrated skew quadrupole strength.

The equilibrium beam emittances are expected to evolve following (the earlier “eq” (equilibrium) subscript has been dropped in the following, for simplicity)

$$\epsilon_x = \epsilon_{x,0} \frac{2|\kappa|^2 + \Delta^2}{4|\kappa|^2 + \Delta^2}, \quad \epsilon_y = \epsilon_{x,0} \frac{2|\kappa|^2}{4|\kappa|^2 + \Delta^2} \quad (29)$$

and their ratio is expected to satisfy

$$\frac{\epsilon_y}{\epsilon_x} = \frac{|\kappa|^2}{|\kappa|^2 + \Delta^2/2} \quad (30)$$

The sum of the transverse emittances is expected to be invariant, equal to the natural horizontal emittance,

$$\epsilon_x + \epsilon_y = \epsilon_{x,0} \quad (31)$$

5.2 Typical data out of Zgoubi

A first numerical experiment is performed at 6 GeV energy.

The working conditions are summarized in Tab. 8. A 5000 particle bunch is tracked for 20000 turns, *i.e.*, 15 emittance damping times about. Eq. 40 still holds in deriving emittances from the particle coordinates, since the coupling does not change the horizontal dispersion, and in particular $D_x = 0$, $D'_x = 0$, at the observation point. The results of the tracking are displayed in Fig. 8. Matching of the exponential decay towards the horizontal and vertical emittances yields the three numerical values for the equilibrium emittances in the bottom row in Tab. 8, differing respectively by less than 1%, 5% and 4% from the expected values, rightmost three columns in Tab. 8.

5.3 Emittance ratio and sum

This second exercise is performed at higher energy, 18 GeV (for the sake of computing speed, essentially). Series of 5000 particles are tracked for 800 turns, *i.e.*, 15 emittance damping times about. The tracking is iterated for a series of values of the coupling strength $|\kappa|$ at fixed distance Δ from the tune diagonal. The working conditions

Table 8: Coupling simulations and tracking results. The left two columns give the unperturbed tunes, the third one gives their distance to an integer. The rightmost four columns give respectively the expected uncoupled natural emittance $\epsilon_{x,0}$ (from the formula in Tab. 6), the expected equilibrium emittances (Eq. 29) and their ratio (Eq. 30). The equilibrium emittances and their ratio from an exponential fit of the tracking data (as displayed in figure 8) are given in the bottom row, rightmost four columns, for comparison.

$\Delta =$							equilibrium emittances, ratio			
Q_x	Q_y	$ Q_x - Q_y - 25 $	$ K_s L $ (m ⁻¹)	β_x (m)	β_y (m)	$ \kappa $	$\epsilon_{x,0}$	ϵ_x	ϵ_y	ϵ_y/ϵ_x
							(nm.rad)			
36.203	11.198	5 10 ⁻³	1.5 10 ⁻³	26.6	11.3	4.2 10 ⁻³	6.83	4.34	2.49	0.575
							6.83	4.31	2.38	0.557

are, paraxial, unperturbed : $Q_x = 36.175$, $Q_y = 11.18$, $\beta_x = 26.5$, $\beta_y = 11.4$. Compared to the previous exercise, the tunes have been moved to a region free of non-linear coupling resonance, see appendix B.3 and Fig. 11.

A summary of the tracking results regarding the ratios in Eqs. 30, 31 is given in figure 9. Tracking data (markers in the figure) are superimposed with these analytical expectations. Up to a strong $|\kappa|/\Delta \approx 5$, $(\epsilon_x + \epsilon_y)$ falls within $\pm 5\%$ of $\epsilon_{x,0} \approx 65$ nm.rad. Beyond that limit, $(\epsilon_x + \epsilon_y)/\epsilon_{x,0}$ increases, the reason for that requires further investigation, however, as opposed to the perturbative hypothesis above, strong coupling substantially changes the optical functions and tunes [19, 20], the latter are moved away from one another, being the coupling strength the minimum tune separation (that effect can be quantified from a Fourier analysis of Zgoubi tracking data).

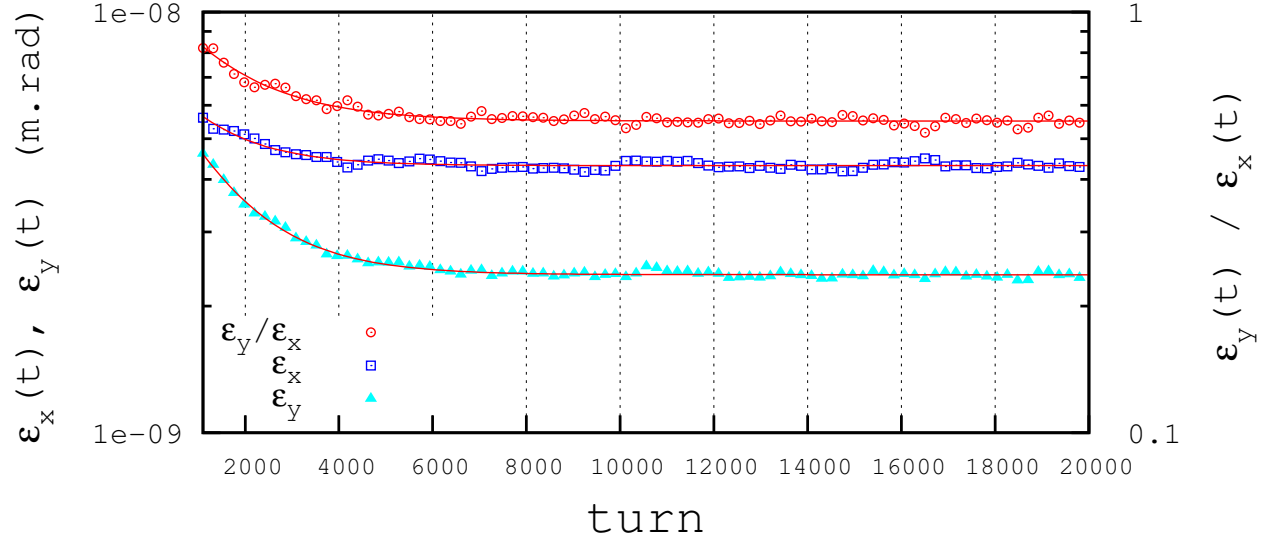


Figure 8: Evolution of horizontal and vertical emittances with turn, in presence of coupling (left vertical axis), and their ratio (right axis). Markers are from Zgoubi tracking. An exponential fit (solid curves) yields the asymptotic values in Tab. 8, bottom row. (Emittance values from tracking are reported only every other 200 turns about on this plot).

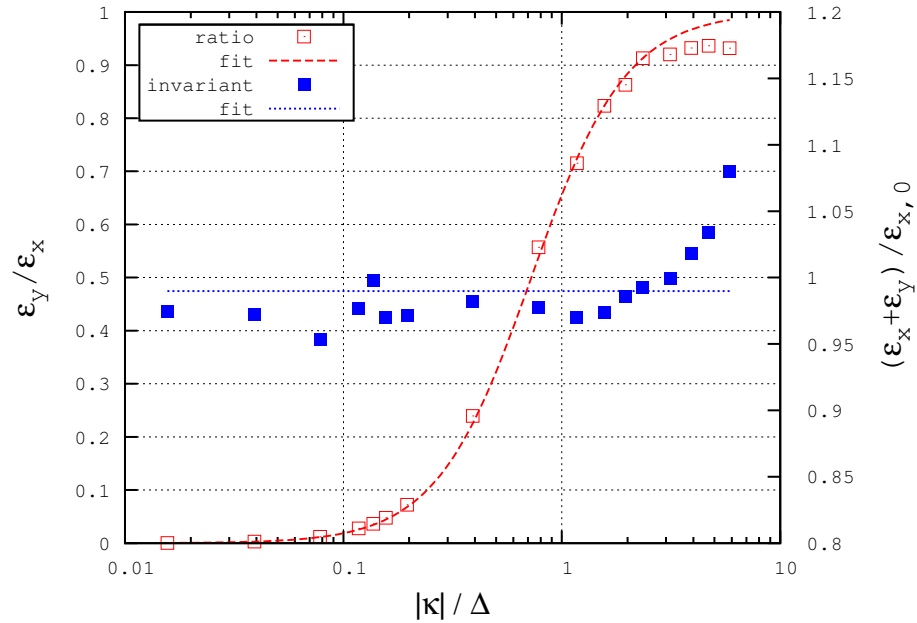


Figure 9: Left vertical scale : evolution of the ratio of vertical to horizontal equilibrium emittances with coupling strength, from Zgoubi tracking (empty red markers), and their interpolation using equation 30 (red “fit” curve). Right scale : $(\epsilon_x + \epsilon_y)/\epsilon_{x,0}$ ratio at equilibrium as a function of coupling strength, from tracking (solid blue markers) and their average value (horizontal dashed blue line).

6 Comments / conclusions

Stepwise ray-tracing of 6-D motion in Zgoubi in presence of SR has been investigated in many aspects, including conditions of coupled optics. Numerical values have been put on many theoretical quantities as energy loss, damping times, equilibrium emittances, and appear to yield reasonable agreement, so bringing confidence regarding the correctness of the Monte Carlo SR machinery installation on the one hand, and on the accuracy of the numerical tracking in presence of SR and its stochastic effects on beam dynamics, on the other hand.

However, it is left to future users, consistently with the particular usage that might be made of Zgoubi, to check further the many aspects that have been left over, as for instance, beam dynamics in presence of synchrotron radiation in all magnets, effects of angle scattering, coupling in the presence of overlapping resonances, etc.

A conclusion that can be drawn from the present investigations is that no unexpected result was obtained, neither any show stopper faced, all the simulations undertaken have given expected data within reasonable accuracy margin.

Further, the computational material for the investigation of SR induced spin diffusion is operational, a follow on of the present benchmarking studies will essentially be a matter of further spin dynamics simulations in the presence of stochastic energy loss.

APPENDIX

A Simulation of energy loss

Probability of emission of a photon Given that the number of photons, k , radiated within an integration step Δs is normally small (units or fraction of a unit) ³ a Poisson law

$$p(k) = \frac{\Lambda^k}{k!} e^{-\Lambda} \quad \text{with} \quad \Lambda = \langle k \rangle, \Lambda = \langle (\Delta k)^2 \rangle \quad (32)$$

is accounted for. The average number of photons over an integration step expresses as ⁴

$$\langle k \rangle = \Lambda = \frac{5er_0}{2\hbar\sqrt{3}} \beta^2 B\rho \frac{\Delta s}{\rho} \quad (33)$$

with $r_0 = e^2/4\pi\epsilon_0 m_0 c^2$ the classical radius of the particle of rest-mass m_0 , e the elementary charge, $\hbar = h/2\pi$, h the Planck constant, $\beta = v/c$, $B\rho$ the particle stiffness, ρ the local curvature radius. At each integration step, Λ is first evaluated from the current values of β , $B\rho$ and Δs , then a value of k is drawn from Eq. 32 using a rejection method.

Energy of the photons These k photons are assigned energies $\epsilon = h\nu$ at random, in the following way. The cumulative distribution of the energy probability law $p(\epsilon/\epsilon_c)d\epsilon/\epsilon_c$, *i.e.*, the probability that the photon has its energy in $]0, \epsilon]$, writes

$$\mathcal{P}(\epsilon/\epsilon_c) = \frac{3}{5\pi} \int_0^{\epsilon/\epsilon_c} \frac{d\epsilon}{\epsilon_c} \int_{\epsilon/\epsilon_c}^{\infty} K_{5/3}(x) dx \quad (34)$$

with $K_{5/3}$ the modified Bessel function, $\epsilon_c = 3\hbar\gamma^3 c/2\rho$ the critical energy of the radiation. The latter is evaluated at each integration step ⁵ from the current values of γ and ρ . In the low frequency region (*i.e.*, in a practical manner, $\epsilon/\epsilon_c < 10^{-2}$), $\mathcal{P}(\epsilon/\epsilon_c)$ (Eq. 34) is approximated in Zgoubi (at better than 1% precision) using

$$\mathcal{P}(\epsilon/\epsilon_c) = \frac{12\sqrt{3}}{2^{1/3} 5 \Gamma(\frac{1}{3})} (\epsilon/\epsilon_c)^{1/3} \quad (35)$$

Beyond, over $10^{-2} < \epsilon/\epsilon_c \leq 10$, $\mathcal{P}(\epsilon/\epsilon_c)$ is interpolated from a set of 40 values that have been tabulated in Zgoubi source software.

Thus, In order to get ϵ/ϵ_c , a random value $0 < \mathcal{P} \leq 1$ is first generated uniformly, then ϵ/ϵ_c is drawn from Eq. 35 if $\mathcal{P} < 0.26$, or by inverse linear interpolation from the tabulated values if $\mathcal{P} > 0.26$.

Note that - a checking means, see Tab. 1 - in a uniform magnetic field the statistics is expected to converge towards the following ensemble averages (SI units) :

- critical energy $\epsilon_c = 3\hbar\gamma^3 c / 2\rho$,
- average photon energy $\bar{\epsilon} = 8\epsilon_c / 15\sqrt{3}$,
- *rms* energy spread $\left(\overline{\epsilon^2} - \bar{\epsilon}^2\right)^{1/2} = \sqrt{211/675} \epsilon_c$,
- number of average photons per particle $= \Delta E / \bar{\epsilon}$.

³For instance, a 10 GeV electron will radiate on average $\Lambda = 20.038 E[GeV] \times \Delta\theta \approx 206 \times \Delta\theta$ photons over a step $\Delta s = \rho\Delta\theta$, *i.e.*, about 2 photons for a 10 cm step under the effect of a 10 m radius bending.

⁴This leads for instance to the usual formula for electrons : $\Lambda/\Delta\theta[rad] \approx 129.5E[GeV]/2\pi \approx \gamma/94.9$.

⁵From a practical viewpoint, ρ is obtained from the value of the magnetic field computed for a one-step push of the particle, following what, SR loss corrections are applied.

B Chasman-Green test lattice

B.1 Properties

A Chasman-Green cell (aka double-bend achromat, DBA) is considered in the present benchmarking study, for the reason that a number of quantities relevant to beam dynamics under SR effects can be derived analytically in that case, as the chromatic invariant \mathcal{H} , equilibrium emittances, damping times, etc.

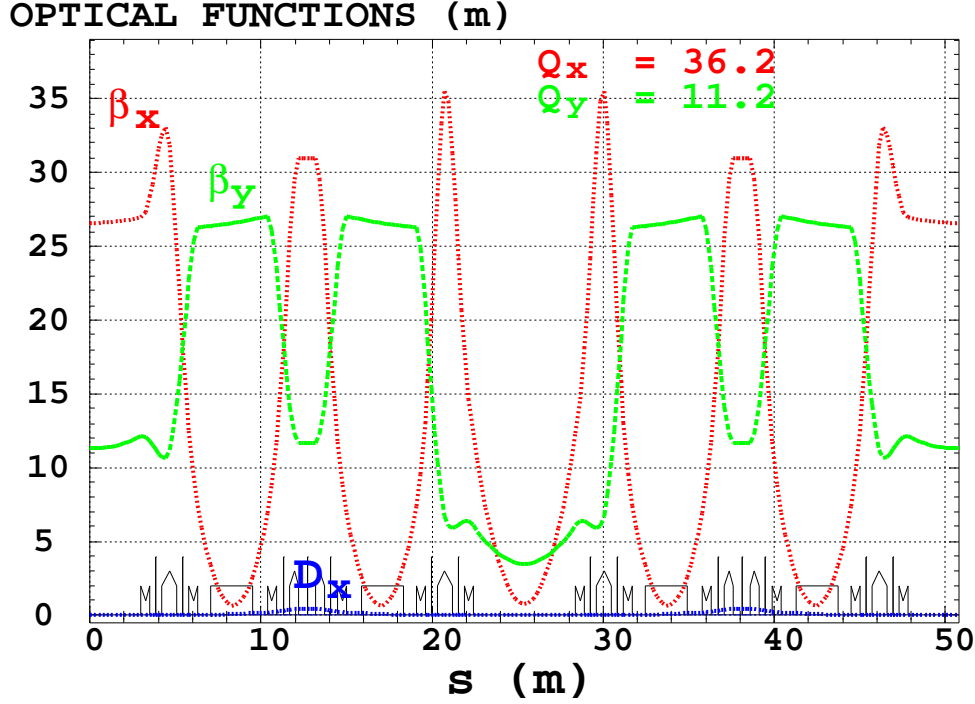


Figure 10: Optical functions in the Chasman-Green cell.

A variant of the ESRF super-cell (a double-DBA) is used, a storage ring is built from 16 such super-cells, whereas various storage energies will be considered, taken in the range 6 GeV (actual ESRF energy) to 18 GeV.

Tab. 9 gives the general optical parameters of the lattice and ring, the optical functions are displayed in figure 10.

B.2 RF conditions

SR losses in bends over the ring circumference amount to

$$U_s = \frac{C_\gamma}{2\pi} \beta^3 E_s^4 I_2 \approx \frac{C_\gamma}{2\pi} E_s^4 I_2 \stackrel{iso-\rho}{=} C_\gamma \frac{E_s^4}{\rho} \quad \text{or, ultra-relativistic electrons,} \quad U_s [keV/turn] \approx 88.463 \frac{E_s^4 [GeV]}{\rho [m]}$$

yielding for instance

$$U_s \approx 4.6 \text{ MeV/turn at 6 GeV, } 2.45 \text{ MW power}$$

Numerical values, for 6 GeV electrons, are given in Tab. 1. The radiated energy is restored by the RF system. A single cavity is accounted for in the present simulations, with parameters as listed in Tab. 10.

Table 9: Ring parameters, as set in the tracking simulations, and other numerical data used in the main text as obtained from Zgoubi tracking. Corrected chromaticities are accounted for in the present benchmarking simulations.

1	Cell length	(m)	50.800
2	Number of cells		16
3	Circumference, $\mathcal{C} = 2\pi R$	(m)	812.800
4	momentum compaction, α	(10^{-4})	3.098
5	Q _x		36.20
6	Q _y		11.20
7	Q' _x , Q' _y , natural		-114, -34.5
8	Q' _x , Q' _y , corrected		+0.035, -0.012
<i>Bend parameters :</i>			
9	Nb. of bends		64
10	Bend deviation, θ	(rad)	$2\pi/64$
11	Bend length, \mathcal{L}	(m)	2.45
12	Curvature radius, ρ	(m)	24.95549
<i>Periodic functions at non-dispersive dipole end :</i>			
13	β_0	(m)	3.415
14	α_0		2.073
<i>Periodic functions at $s=0$:</i>			
15	β_x, β_y	(m)	26.6088, 11.3027
16	α_x, α_y		0

Table 10: RF conditions in Zgoubi simulations, longitudinal parameters.

Revolution time, T_{rev}	($10^{-6}s$)	2.71122
Frequency, $f_{rf} = \omega_{rf}/2\pi$	(MHz)	110.651
Harmonic, h_{RF}		300
Synchronous phase, φ_s	(deg)	30
Peak voltage, \hat{V}	(MV)	$9.19123 \times \left(\frac{E_s[GeV]}{6.000511} \right)^4$
Synchrotron tune, Q_s		$0.004430 \times \left(\frac{E_s[GeV]}{6.000511} \right)^{3/2}$

B.3 Coupled optics

The precise positioning of the working point is not a concern in the non-coupled numerical experiments, first part of the note, since there is no source of non-linear coupling excitation, apart from kinematic terms present by nature in the Zgoubi method, however negligible given the paraxial working conditions. That working point happens to be located at (A), Fig. 11.

By contrast, in the case of the coupled optics the working point is located in a resonance line free diamond, point (B) in Fig. 11. This is in order to fulfill the coupling formalism hypothesis of an isolated linear coupling resonance. Chromaticities are below 0.1 so ensuring small footprint well within the resonance-free diamond.

Note that it has been observed that, performing similar coupling simulations with working point (A) instead, straddling sum coupling resonance lines, jeopardizes the invariance of $\epsilon_x + \epsilon_y$ when $\kappa/\Delta \gtrsim 0.5$, to be compared to similar effect for $\kappa/\Delta \gtrsim 5$ instead, with working point (B),

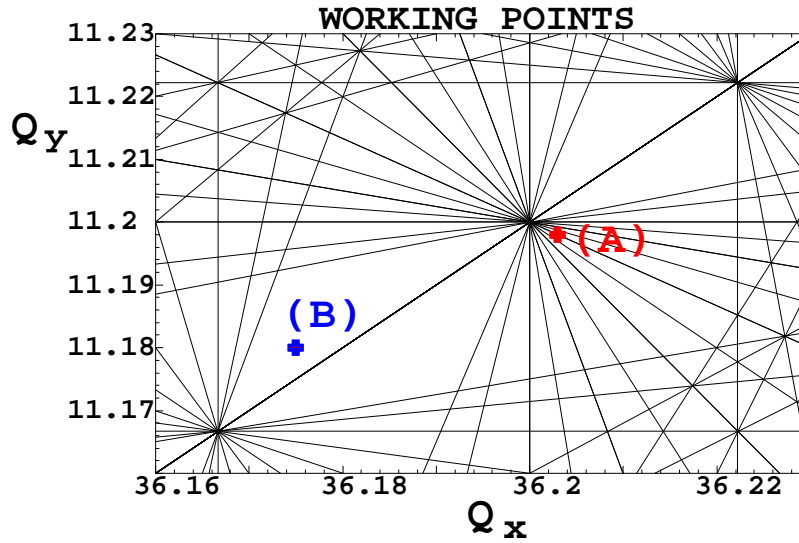


Figure 11: Working points. (A) uncoupled case. (B) coupled case, away from coupling resonance lines $mQ_x + nQ_y = p$, p integer, represented up to order $|m| + |n| = 10$ here.

C Numerical convergence

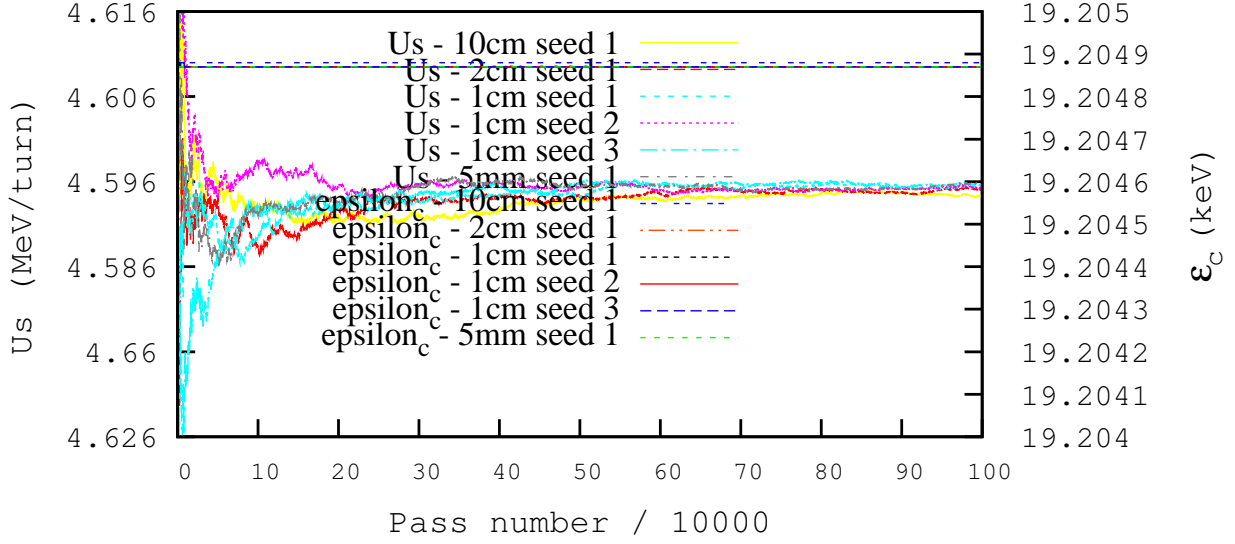


Figure 12: Convergence (running average) of the energy loss towards 4.5956 MeV/turn (lower curve bundle, left vertical scale), and of the critical frequency towards 19.205 keV (top curve bundle, right vertical scale), as a function the number of passes of a 3000 particle batch, through the 2.45 m dipole, at 6 GeV.

In order to perform a preliminary convergence test on the Monte Carlo SR loss installation in Zgoubi, a 3000 particle batch is launched for a large number of passes through a single dipole of the Chasman Green cell. The dipole is 2.45 m long (Tab. 9), the test is performed at 6 GeV kinetic energy. Figure 12 displays the results of a series of trials, involving various random seeds, various integration step size in the bend. It shows, (i) that both the energy loss U_s and the critical energy ϵ_c converge to their asymptotic values in a few once-through passes across the dipole, (ii) that energy loss values are in accord with theoretical expectations (Tab. 1, rightmost column) at ppm level at all four tested energies, see numerical data in Tab. 7, second column.

D Concentration ellipses

Series of comparisons discussed in this report lean on the concentration ellipses, which are a standard product out of Zgoubi and its data treatment/analysis interface zpop [2]. In order to make things clear, we recall briefly the way they are computed in the code, from the coordinates of the particles.

Let $z_i(s)$, $z'_i(s)$ be the phase space coordinates of $i = 1, n$ particles observed at some azimuth s , at some turn around the ring. The second moments of the particle distribution are

$$\begin{aligned}\overline{z^2}(s) &= \frac{1}{n} \sum_{i=1}^n (z_i(s) - \overline{z}(s))^2 \\ \overline{zz'}(s) &= \frac{1}{n} \sum_{i=1}^n (z_i(s) - \overline{z}(s))(z'_i(s) - \overline{z'}(s)) \\ \overline{z'^2}(s) &= \frac{1}{n} \sum_{i=1}^n (z'_i(s) - \overline{z'}(s))^2\end{aligned}\tag{36}$$

From these, a concentration ellipse (CE) is drawn, of surface $\mathcal{S}_z(s)$ and equation

$$\gamma_c(s)z^2 + 2\alpha_c(s)zz' + \beta_c(s)z'^2 = \mathcal{S}_z(s)/\pi\tag{37}$$

354 Noting $\Delta = \overline{z^2}(s) \overline{z'^2}(s) - \overline{zz'}^2(s)$, the ellipse parameters write

$$\gamma_c(s) = \overline{z'^2}(s)/\sqrt{\Delta}, \quad \alpha_c(s) = -\overline{zz'}(s)/\sqrt{\Delta}, \quad \beta_c(s) = \overline{z^2}(s)/\sqrt{\Delta}, \quad \mathcal{S}_z(s) = 4\pi\sqrt{\Delta} \quad (38)$$

355 With these conventions, the *rms* values of z and z' projections satisfy

$$\sigma_z = \sqrt{\beta_z \mathcal{S}_z / \pi} \quad \text{and} \quad \sigma_{z'} = \sqrt{\gamma_z \mathcal{S}_z / \pi} \quad (39)$$

356 In addition, in the first order formalism, given that the observation point in these simulations is taken in a non-
357 dispersive region ($s = 0$ in Fig. 10), the CE surface identifies with the emittance,

$$\mathcal{S}_z(s) \equiv \epsilon_z \quad (40)$$

References

- [1] F. Méot, The ray-tracing code Zgoubi, Nucl. Inst. Meth. A 427 353-356 (1999).
- [2] The Zgoubi user manual can also be found at
<http://www.scienceaccelerator.gov/dsa/result-list/fullRecord:zgoubi/>
 Source files and examples are available at <http://sourceforge.net/projects/zgoubi/>
- [3] F. Méot, J. Payet, Numerical tools for the simulation of synchrotron radiation loss and induced dynamical effects in high energy transport lines, internal report DAPNIA/SEA-00-01, CEA/DSM Saclay (July 2000).
- [4] P. Lapostolle, F. Méot, S. Valero, A new dynamics code DYNAC for electrons, protons and heavy ions in LINACS with long accelerating elements, 1990 LINAC Conf., Albuquerque, NM, USA ; report SATURNE/GT/90-04, CEA/DSM Saclay (1990).
- [5] Electron Laboratory For Europe, “Blue Book” Accelerator Technical Proposal, CNRS-IN2P3 editor, Institut des Sciences Nucléaires, Grenoble, France (1994).
- [6] G. Leleux, P. Nghiem, A. Tkatchenko, Synchrotron radiation perturbation in transport lines, IEEE 1991 Particle Accelerator Conference, San Francisco, USA, May 6-9, 1991.
- [7] V. Ptitsyn et al., High luminosity electron-hadron collider eRHIC,
<http://accelconf.web.cern.ch/AccelConf/IPAC2011/papers/thpz019.pdf>.
- [8] F. Méot, A numerical method for combined spin tracking and ray tracing of charged particles, NIM A 313 (1992) 492-500.
- [9] F. Méot et al., Lattice design and study tools regarding the super-B project, Procs. IPAC10, Kyoto, Japan, 2010.
- [10] F. Méot, End-to-end 9-D polarized bunch transport in FFAG eRHIC,
 EIC14 workshop, <http://www.jlab.org/conferences/eic2014/>.
 F. Méot, V. Ptitsyn et al., Extensive end-to-end simulations of bunch and polarization transport in the eRHIC energy-recovery collider, Submitted to IPAC14.
- [11] C. Bovet, A. Burns, F. Méot, M. Placidi, E. Rossa, J. De Vries, Synchrotron radiation interferences between short dipoles at LEP, rep. CERN SL/97-59 (BI), Nov. 1997. <http://www.osti.gov/scitech/biblio/562080>.
 F. Méot, A theory of low frequency, far-field synchrotron radiation, Particle Accelerators, Vol. 62 (1999), pp. 215-239.
- [12] L. Ponce, R. Jung, F. Méot, LHC proton beam diagnostics using synchrotron radiation, Yellow Report CERN-2004-007.
- [13] L. Ponce, F. Méot, Undulator radiation simulation tools in view of proton beam diagnostics in LHC, SL-Note-2001-038/BI, CERN, 25 Sept. 2001.
- [14] F. Méot, A. Verdier, Effect of the undulator in IR4 on the LHC beam, CERN LHC Project Note 343 (2004).
- [15] F. Méot et al., Polarization transmission at RHIC, numerical simulations, Proceedings of IPAC2012, New Orleans, Louisiana, USA.
 F. Méot et al., Spin code benchmarking at RHIC, Proceedings of 2011 Particle Accelerator Conference, New York, NY, USA.

- 395 [16] F. Méot et al., Spin tracking simulations in AGS based on ray-tracing methods, internal report C-AD/AP/452,
396 Sept. 2009.
- 397 [17] M. Sands, The Physics of Electron Storage Rings: An Introduction, SLAC Report 121 (1970). Available at
398 <http://www.slac.stanford.edu/pubs/slacreports/slac-r-121.html>
- 399 [18] L. Farvacque et al, BETA users' guide, ESRF, third edition (2001).
400 https://oraweb.cern.ch/pls/hhh/code_website.disp_code?code_name=BETA
- 401 [19] G. Guignard, Betatron coupling and related impact of radiation, Phys. Rev. E 51 61046118 (1995).
- 402 [20] Y. Luo, Transverse beam sizes and quasi emittances for linear coupled optics, NIM A 562 (2006) 57-64.